TECHNIQUE STANDARDIZATION TO ACHIEVE CONSISTENT IMAGE QUALITY FOR SCOLIOSIS PATIENTS

By

Joseph V. Belobrajdich

A THESIS

Presented to the Department of Medical Physics
and the Oregon Health & Science University
school of Medicine
in partial fulfillment of
the requirements for the degree of

Master of Science

June 2019

School of Medicine

Oregon Health & Science University

CERTIFICATE OF APPROVAL

This is to certify that the Master's thesis of

JOSEPH VINCENT BELOBRAJDICH

Has been approved

____
Mentor/Advisor

____
Member

____
Member

____
Member

Table of Contents

Figures, Tables and Equations

Acknowledgements

I would like to personally thank Dr. Thomas Griglock for his immense patience with me and guidance with this project. More importantly however, thank you for your personal guidance and reassurance that I will be able to find my place in this incredible field. I also want to express my gratitude to Dr. Lindsay DeWeese for her invaluable guidance and for challenging me and to strive for excellence.

Thank you to my classmates who have made my stay in Portland an amazing and wonderful experience. I eagerly look forward to addressing you as colleagues in the near future.

While she is no longer with us in the department, I would also like to thank Dr. Krystina Tack for her advising, personal guidance and encouragement to persevere in my graduate studies.

Sincerely,

Joe Belobrajdich

Abstract

Introduction

The aim of this project is to develop consistent exposure technique guidelines for imaging scoliosis patients with radiography. Scoliosis is the condition where a spine exhibits lateral curvatures deviating from the midsagittal plane [1], [2]. The vast majority of scoliosis cases have unknown etiology with typical treatment methods involving monitoring of the patient's condition for any exacerbating effects [2]. Monitoring of the patient's condition is done using radiographic images. Commonly used imaging methods equipped with automatic exposure control are not available to this patient population owing to the large field of anatomy required for imaging. This project standardizes technique methods for the technologist to ensure consistent noise content in images. Exposure Index (EI) values serve as a guiding metric for both techniques and image quality as EI is linearly proportional to the incident detector air kerma and is proportional to the square of the signal to noise ratio [17].

Methods

Factors such as patient thickness, source to image distance (SID), and room output were incorporated in developing these techniques. A modified American National Standard Institute (ANSI) phantom consisting of acrylic and 1100 alloy aluminum was used to simulate the thickest portion of anatomy. The phantom thickness was adjusted to account for variability in anteroposterior measurements in patient size and the SID was adjusted to account for variations

in patient height. Images with EI values from 400 to 500 are regarded as having appropriate noise level content. Therefore, this range served as the target EI range. Half value layers (HVL) determine the effective energy of a polyenergetic beam and were measured in order to determine patient equivalent thicknesses for the phantoms used. Tube outputs were also measured to translate techniques from one room to another.

Results

Initial experiments found that calculated EI values were dependent upon exam protocols and CR cassettes. All but one of the finalized techniques showed average EI values ranging from 407 to 501.25. The largest phantom at 90” SID exhibited an unusual $730.\overline{6}$ average EI value. The results indicated that the method was suitable for all configurations excluding the 38 cm phantom at an SID of 90” for both rooms tested. Tube output ratios from room B to room C were between 0.856 and 0.929, and the resultant average EI values for room C ranged from $313.\overline{6}$ to 498.5 for finalized techniques. For room B, calculations based on HVL measurements showed that the thinnest phantom was equivalent to a patient whose maximum anteroposterior measurement was 13.96 cm. The largest phantom was equivalent to a maximum anteroposterior measurement of a 36.98 cm patient. Room C showed 14.62 cm and 37.28 cm patient equivalencies for the small and large phantoms respectively.

Conclusion

The results showed that the exposure index could be utilized as a means of obtaining consistent noise content in images in addition to determining technique factors for varied phantom thicknesses.

1. Introduction

The human vertebral column naturally follows four curvatures along the mid-sagittal plane. These are the cervical, thoracic, lumbar and sacral curves. Scoliosis is the condition in which the vertebral spine exhibits curvatures beyond the mid-sagittal plane [1], [2]. Typically these curvatures are readily observed in the coronal planes but may exhibit more tortuous paths through other dimensions [2]. The Cobb angle is a measurement describing the maximum deviation the spinal column has from the mid-sagittal plane. Scoliosis is a condition more commonly found in adolescent patients with approximately three million expected new cases each year in the United States alone [3].

The biomechanical progression of scoliosis appears in two distinct stages. The first is curve initiation followed by progression [4]. Factors influencing these stages appear to be driven by compressive and tensile forces on the vertebral plates during the phase of skeletal immaturity; a phase attributable to all adolescents. A compressive force pushes vertebral plates together and minimizes the vertebral disk space while the tensile force pulls the plates apart, expanding disk space. Bone growth is hindered by compressive forces while growth is accelerated by the tensile forces. This process of bone growth and cessation of growth is referred to as the Hueter-Volkmann law [2]. In a normal thoracic spine curve, the compressive force acts on the ventral edge of the vertebral plate while the tensile force acts on the dorsal end [2].

A leading hypothesis for abnormal development of spinal curvatures postulates that the vertebral plates are rotated in the axial plane thereby causing uneven and mismatching of the compressive and tensile forces at play in the vertebral column. This misalignment of forces leads to a deviation of the normal spine curvature, resulting in curvatures that manifest outside of the mid-sagittal plane [5]. Figure 1, illustrates the compressive and tensile forces acting on the vertebral plates [5]. Once a certain level of curvature has formed, the progression of scoliosis accelerates, especially during the phases of rapid spinal growth [6]. Primary curves are the largest and first abnormalities to develop during this process. Secondary curves then follow as additional less severe curvature

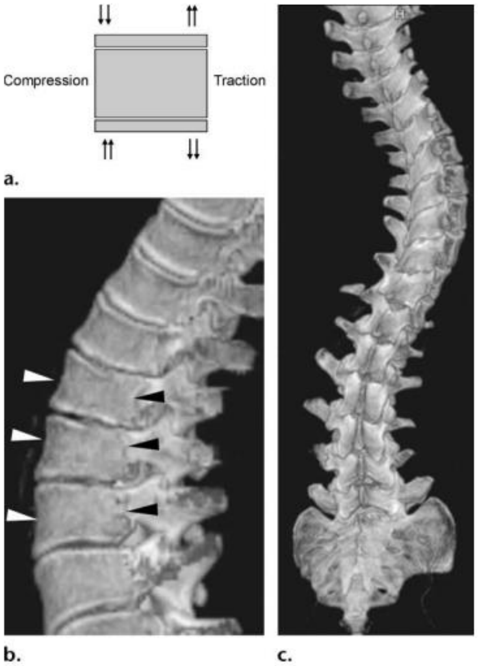

Figure 1 An anatomical portrayal of both compression and traction forces acting on the vertebral discs. A) Force vectors illustrating compression and traction on vertebral disks. B) The white arrows indicate regions of compression while black arrows depict regions of traction. C) Portrays scoliosis with a 3D CT image. Note the tortuous curvature of the spine in three dimensions[2].

progressions in order to compensate for the loss of balance that is produced from the primary curvature [5].

There are two etiologic classifications of scoliosis; primary and secondary. For primary conditions, scoliosis is further characterized by the patient's age. Primary classification of scoliosis is also referred to as idiopathic scoliosis for which the underlying cause is unknown. Infantile idiopathic scoliosis is categorized for patients at the age of three or younger. Levoscoliosis refers to a lateral curvature in the left sagittal plane while dextroscoliosis refers to the curvature extending into the right sagittal plane. The vast majority are male patients with levoscoliosis being more common than dextroscoliosis. Juvenile idiopathic scoliosis encompasses the age group of patients from four to ten years of age. Most of this category is composed of female patients with dextroscoliosis being more common than levoscoliosis. The third subcategory of idiopathic scoliosis is adolescent scoliosis which spans the age group from ten to eighteen years of age [1], [5].

While idiopathic primary scoliosis is subdivided according to the patient's age, secondary scoliosis is subcategorized by underlying causation [5]. The Scoliosis Research Society further divides secondary scoliosis into the categories of congenital, developmental, neuromuscular, and tumor associated [5], [6]. Eighty percent of cases are classified as idiopathic, meaning the vast majority of cases have an unknown etiology. Ten percent of cases are classified as secondary congenital, and neuromuscular, and developmental. Scoliosis conditions with tumors as the underlying causation account for the remainder ten percent of cases [2]. It is worth mentioning that conditions for which a patient exhibits a forward fold in their upper vertebral column is defined as kyphosis while lordosis is defined by lower excess curvature of the lumbar spine [7]. These are further classified into subcategories [5], but are not addressed in this thesis.

Proper identification of apex curves, significant vertebrae as well as classification of scoliosis are essential to ensure quality patient care [5], [7]. Apex vertebra are defined as the vertebral disks either farthest deviated from the central vertebral line or the disk with the greatest offset rotation in the axial plane. End vertebrae are defined as the vertebral disks with the greatest tilt in the coronal plane and are used for Cobb angle measurements [8]. The central sacral vertical line is drawn orthogonally to a line tangential to the peaks of the patient’s iliac crests and is often abbreviated CSVL. Neutral vertebrae are those exhibiting no rotation and stable vertebrae are the discs farthest from the skull that are bisected or nearly bisected by the central sacral vertical line. Laterally, the CSVL

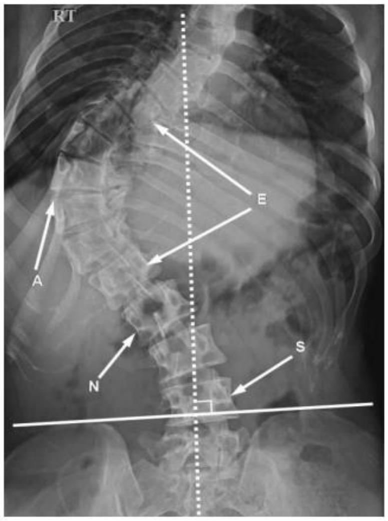

Figure 4 Sample radiograph showing stable (S), Neutral (N), Apex (A) and End (E) vertebrae. Stable implies that the vertebra is very nearly bisected by the CSVL. Neutral vertebrae are those without axial rotation. The Apex is the point farthest from the CSVL. End vertebrae are those with the highest degree of tilt.

bisects the sacrum. Figure 2 illustrates these components and their application to a sampled patient with scoliosis [9].

Cobb angle measurements are inherently challenging in radiography in part due to a three dimensional structure being displayed as a two dimensional image. Any rotation of the vertebral discs is thereby hidden in the image [10]. Additionally, it is often difficult to position patients with an accurate frontal view such that successive follow up measurements can accurately assess progression [5], [7]. Surgeons have also reported that patients in prone position exhibit a decreased Cobb angle than when measured in the upright position in radiography. Sometimes, after surgery has been performed and upon the patient’s return to the upright position, a postoperative ‘rebound effect’ ensues with a loss of planned correction [7], [11]. For these reasons and others, it is imperative that consistent nomenclature of the vertebral disks and careful measurements be made for this patient population. Despite these drawbacks, Cobb angle measurements still serve as the standard for demarcation of the disease as well as monitoring progression [5], [7].

Idiopathic scoliosis is usually diagnosed after all other possible causes have been dismissed [7]. Radiography is used to initially diagnose this disease due to its adequacy of determining most congenital and developmental osseous deformities. However, CT and MRI are employed to investigate further underlying causes not deducible from a radiographic scan. These usually involve cases where an osseous tissue or nervous tissue deformity is observed or suspected [5], [7].

Radiography however serves as the foremost imaging modality for this patient population [6]. This is in part due to its adequacy in ruling out the majority of other causes that would otherwise require CT or MR imaging. More importantly, monitoring of the patient’s condition is evaluated by the measurement of Cobb angles which radiographic images adequately supply. It is the monitoring and measurement of these angles upon which physicians prescribe treatments for these patients [5], [7].

1.1 Radiography and Image Quality

Radiography makes use of photons to produce radiographic images. These are produced primarily through bremsstrahlung radiation when electrons in a tube current bombard a target anode. The resulting interactions cause the electrons to decelerate, therefore producing an electromagnetic wave, also called x-rays or photons. For an overview of how these photons or x-rays are produced, the reader is referred to appendix A.

The photons that leave the x-ray tube then interact with the patient. In diagnostic radiography, interactions between photons released from the x-ray tube and matter particles composing the patient are: Rayleigh scatter, Compton scatter, and the Photoelectric effect [13]. The probability of interactions of these events are dependent upon the energies of the interacting photons as well as the atomic number of the absorbing tissues in the patient [12], [13].

Rayleigh scatter, also referred to as coherent scatter, results in the near negligible loss of energy of the interacting photon. Essentially, there is no significant exchange of energy between photon and atom which implies that there is no kerma, dose, ionization, or excitation of any particle or nucleus. The traversing photon is considered non-attenuating and does not contribute any useful information towards image quality in radiography or dose to the patient due to lack of interactions [13].

Compton scatter, or incoherent scatter, is the direct interaction between a valence electron and a photon under the assumption that there is no binding energy associated with the at rest electron. During this interaction, a photon strikes a free electron imparting some of its energy to the electron. This results in a decrease of the photon's final energy state as well as a change in its original direction or scatter [13].

Many Compton events occur within the human body during a radiography exam with various degrees of scatter. This results in a spectrum of energy distributions in the finalized energy states of the photons that are eventually incident on the detector. Since a variety of finalized photon energy states reach the detector, the detector's response is also varied. As a consequence, Compton scatter contributes noise in radiographic images [12], [13].

The photoelectric effect occurs when a photon releases an electron originally bound to a material. In this interaction, a photon must have sufficient energy to free an electron and any excess energy transfers to the kinetic energy of the electron [12], [13]. Of all these interactions, the photoelectric effect produces the best information in radiography. This is because emitted electrons leave a vacancy within the atoms. What follows are characteristic x-rays which are uniquely valued photons depositing a characteristic energy onto a detector plate. On a macroscopic level, numerous characteristic x-rays emitted from bone will be of a different energy than say the characteristic energies of those emitted from a soft tissue [12]. These differences in energies translate to two distinct responses of the detector and consequently produces contrast in an image [12]. The takeaway from these interactions is that Compton events produce noise in a radiographic image while the photoelectric effect provides contrast in an image.

Technologists utilize both tube potential and current time products to drive these interactions and image quality. Since these interactions are predominantly energy driven, higher tube potentials produce higher energy x-rays which translates to decreased contrast in an image [12]. Tube current measured in milliamps mA, determine the number of photons produced during an exposure. The current time product milliamp-second, mAs, is another technique parameter describing both the time interval a current is used as well as the total charge. Higher mAs values result in more photons reaching the detector which decreases noise in an image [12].

1.2 Issues with Scoliosis Imaging

In radiology, it is essential that all images have consistent noise. Underexposed images have higher noise levels that may obscure subtle details while overexposed images, having less noise, and involve higher dose to the patient [22]. Having established techniques that balance noise with dose to the patient is considered good practice [14]. This is usually achieved either by an automatic exposure control system where an x-ray tube ceases production of photons once an appropriate number reaches the detector. This is common with most imaging examinations such as standard chest x-ray examinations. Another option normally available to technologists is a technique chart where specified kVp and mAs values are provided so that the appropriate image quality for that imaging exam is produced.

Scoliosis imaging requires a larger range of anatomy to be visualized that is not readily accommodated on typical detectors. In these exams, the base of the skull and the pelvis are required on the same image [7]. Sectional imaging using a chest bucky is unreliable due to risk of patient motion despite having the benefit of AEC. Motion is difficult to account for in stitching algorithms and can yield inaccurate Cobb angle measurements [15]. While scanning patients in a supine position is possible and for some the only feasible method for imaging, it is preferred to scan with the patient standing as angle measurements are different between standing and supine positions [7].

As a result of these special considerations, scoliosis exams are performed on a separate scoliboard which houses up to three CR cassettes. The reader is referred to appendix C for a brief review of Computed Radiography. The scoliboard allows for the entire anatomy to be imaged in a single exposure reducing motion artifact probabilities. However, there are no automatic exposure controls or technique charts available to the technologist performing these examinations. As a result, scoliosis patients are more likely subject to non-optimal exposures resulting in inconsistent noise content in their images.

Additionally, due to the wide range of anatomy covered in scoliosis imaging, there exists a wide variety of tissues. Perhaps the entire spectrum of matter comprising the human anatomy exists within a scoliosis image with air found in the lungs, a multitude of soft tissues within the abdomen as well as osseous tissues in the chest, pelvis and spine. Additionally, patients vary in height which imply different source to imaging distances (SID) necessary to capture the anatomy. Patients also differ in anteroposterior measurements. This requires different tube potential techniques as appropriate photon energies are required to penetrate the anatomy. To summarize, variables of source to image distances, tissue density, patient height and thickness, make obtaining consistent image quality difficult.

1.3 Using Exposure Indices to Determine Techniques

In order to address these variables, a metric that guides techniques as well as image quality is preferred. Fortunately, such a metric exists and is called an Exposure Index. Historically, clinics that switched from film to digital radiography soon experienced a phenomenon known as “dose creep.” It became apparent to technologists that underexposed images resulted in higher noise content images and that overexposed images resulted in high quality images with lower noise but a higher dose deposited into the patient. For decades, a general trend of increasing techniques to produce better quality images manifested to decrease excess noise in image at the expense of increased dose to patients. IEC Standard 62494-1 and TG-116 were formed to produce an indicator representing the level of exposure reaching the detector for all operators of digital radiography equipment. This was in effort to reduce patient exposure and to provide a tool for technologists to determine if proper techniques were utilized [12], [14], [16].

The Exposure Index (EI), is a dimensionless scalar quantity that in some way, dependent upon the manufacturer, utilizes some statistical parameter describing the incident air kerma on the detector. The IEC Standard 62494-1 defines the EI by the following expression:

$$EI = c \times g(V) \qquad \text{(Equation 1)}$$

where *c* is the scaling factor set to 100 μGy^{-1} and *g(V)* is the equipment specific inverse calibration function[18]. The inverse calibration function is a value representing the quantity of radiation on the detector from a standardized radiation exposure that would produce the same air kerma at the detector surface [22].

The process in obtaining the EI first involves corrections to the raw data including accounting for defective pixels, flat field corrections, and geometric distortions to name a few [21]. These values are then referred to as for processing Q values and are directly related to the exposure of the detector region they represent [22]. IEC 62494-1 then permits the vendor to determine the relevant image region based on the attenuated regions of the beam that are relevant to the exam [14], [18]. The process for which a vendor’s system determines which for processing Q values are relevant to the clinical examination is referred to as image segmentation [22]. From the data, the vendor is then free to utilize a variety of statistical parameters to determine the quantity of radiation on the detector [18]. TG-116 recommends the median value and also specifies the calibration conditions for the exposure index by the procedure described below. The task group recommends the following materials for added filtration: 0.5 mm Cu and 3 to 4 mm of 1100 grade alloy aluminum.

1. The detector is placed as far away from the x-ray assembly as possible with a minimum distance of 100cm. A CR detector must be suspended from the floor by at least 25cm in order to avoid backscatter.
2. Remove all objects that modify the detector response such as grids.
3. An ion chamber is placed midway between the source and the detector with distances measured.
4. The light field surrounding the collimation of the ion chamber must not exceed 2.54cm.
5. With the detector covered in a lead apron, expose the ion chamber with a 70 kVp energy beam and adjust filtration to obtain a half value layer as close to 6.8 mm Al as possible.
6. With the appropriate beam quality reached (RQA5 70 kVp 6.8 mm Al), determine the air kerma at the detector by using the inverse square correction.
7. Adjust the mAs setting until the desired air kerma is in the middle of the detector response range.
8. With the lead apron removed, open the beam collimation to encompass the entire detector and move the ion chamber perpendicular to the x-ray tube axis such that it is positioned

outside the field of view of the detector but still contained within the beam.

9. With an exposure utilizing the appropriate mAs value, determine the air kerma ratio between the initial and final positions of the ion chamber.

The above procedure outlines the calibration method to determine the standardized air kerma at the detector when air kerma ratios of the ion chamber are corrected with the inverse square law [22].

From the calibrated conditions, the air kerma values in a clinical setting are determined by the RQA5 beam that would produce the same exposure. It is for this reason that the air kerma value is referred to as the indicated equivalent air kerma. A single representative value of all air kerma values from the histogram is left to the discretion of the vendor. TG-116 recommends the use of the median value to better represent the data for cases in which outliers within the raw data are present [14], [18], [22]. With the value selected, this representative air kerma value is multiplied by the *c* scaling factor resulting in the exposure index.

The standard also provides a formula for the deviation index (DI) which measures how far off a current exam EI is from a predetermined target EI for that imaging examination [18]. The standard states that if a target EI exists within the system then a DI value should be computed and displayed numerically to the technologist by:

$$DI = 10 \times log\left(\frac{EI}{EI_T}\right) \qquad \textit{(Equation 2)}$$

As defined by the standard, EI is linear with incident detector air kerma [17]. However, for a varied beam quality, the relationship between EI and incident detector air kerma varies as well. It is also worth mentioning that IEC Standard 62494-1 does not contribute to the establishment of target EI values. Rather, target EI values are stored with the American College of Radiography dose index registry as a source for professionals to compare their determined values against other institutions worldwide [17], [18], [22].

Exposure indices are proportional to the signal to noise ratio and linearly proportional to the incident detector air kerma [17]. They are a dimensionless scalar quantity reflective of the remnant radiation incident on the detector [17]. As EI is calculated by a statistical parameter dictated by the vendor [18], it is a metric reflective of the amount of incident radiation on the detector making it a candidate guiding metric for technique factors. Additionally, because EI is also proportional to the signal to noise ratio of an image, EI is also a reflective measure of noise in an image [17]. Therefore, exposure index values could serve as a suitable metric for delineating techniques in scoliosis imaging while accounting for proper noise consistency in images.

1.4 Law of Exponential Attenuation, Mass Attenuation Coefficients and Room Output

Radiation interactions are dependent upon the energy of the interacting photon as well as the atomic number and electron densities of the absorbing medium [12]. The probability of all possible interactions is given by the linear attenuation coefficient, μ with units of 1/cm. When divided by the material density ρ, μ/ρ becomes the mass attenuation coefficient and can be expressed as:

$$\frac{\mu}{\rho} = \frac{\mu}{\rho}Rayleigh + \frac{\mu}{\rho}Photoelctric\ effect + \frac{\mu}{\rho}Compton\ Scatter \qquad \textit{(Equation 3)}$$

for the diagnostic energy range with units of cm^2/g [12]. The mass attenuation coefficient accounts for all the interactions that can occur within a material.

The law of exponential attenuation describes the initial and final intensities of radiation from the source through a given thickness of material [13]. For this project, the law of exponential attenuation will be used to convert from the materials used for the phantom to the appropriate patient equivalent thickness it represents. The law of exponential attenuation is expressed as:

$$I = I_o e^{-(u/p)pt} \qquad \textit{(Equation 4)}$$

Where, I is the final intensity of a beam, I_O is the initial intensity, e is Euler's number, u/p is the mass attenuation coefficient of a material, p is the density of the material and t is the material's thickness [13]. As the mass attenuation coefficient is dependent upon the energy of the photons used, the effective beam energies are determined from the half value layer. A half value layer, or HVL, describes the necessary material thickness to reduce the initial intensity of a radiation beam by half and is dependent on the energy of the radiation beam [13].

Exposure quantifies the amount of charge of one sign produced by ionization of a photon in air per unit mass with SI units of C/kg [13]. One coulomb per kilogram is equivalent to 0.258 mili-Roentgen or 0.258 mR [13]. The amount of exposure per current time product technique produced from an x-ray assembly can be defined as room output with the unit mR/mAs. Room output factors are x-ray room specific. As tubes age, the resultant exposure produced may deviate meaning that the exposure produced between two rooms may be different despite utilizing the same techniques. In order to convert techniques from one room to another the known exposure per mAs must be known.

2. Materials and Methods

This chapter outlines the materials used for this project as well as the procedure prescribed by the methodology.

2.1 Methodology

In order to optimize techniques for scoliosis imaging, sufficient image quality for the largest anteroposterior portion of patient anatomy is required. It is assumed that the thickest portion of the body is the highest attenuating region of the body. It can be reasoned that thinner anteroposterior portions of the patient produce less attenuation implying suitable image quality in those regions for the same technique. Varying patient thicknesses will be represented by varying thicknesses of a phantom emulating the attenuation of an average patient.

For all source to image distances used in these examinations, proper image quality would be determined by the system's exposure index value (EI). Through previous observer studies with Radiologists, it was determined that a suitable EI target range between 400 and 500 would produce an image of acceptable quality. Techniques will be adjusted accordingly for various acrylic block configurations that account for varying patient sizes at each SID.

When consistent EI values are obtained within the target range and the established techniques for these results recorded, the next step is to determine the equivalent soft tissue thickness of the acrylic. A solid-state detector will measure the half value layer to determine beam quality in order to determine the effective energy. The mass attenuation coefficients are obtained from both Appendix D of Bushberg's *Essential Physics of Medical Imaging* [12] and from

NIST.gov. It became necessary to interpolate values as the measured effective energies of the beams used were not listed.

After the soft tissue equivalence is determined, the final technique chart was developed. Technique charts will display the appropriate anteroposterior patient thickness for a given beam energy and tube current-time product (i.e. kVp and mAs). Techniques will also include the adjusted mAs values for different source to image distances used due to the inverse square law.

The conversion of one room’s technique chart to another will be done by accounting for the tube output of the initial room tested and comparing this output with another room. Tube outputs are measured in mR/mAs and defined as exposure per unit tube current-time product. A solid-state detector was used to determine the output. With the measured tube outputs of another room, it was to be determined if the ratio of tube outputs could accurately predict the mAs techniques of a new room. The tube outputs measured in mR/mAs would determine the mAs needed by taking the ratio of the tube outputs of the two rooms multiplied with the mAs of the original room.

2.2 Materials

The materials for this project involved an AGFA system radiography room equipped with a scoliosis board capable of housing up to three computed radiography cassettes. An AGFA CR reader was necessary for image processing of the CR cassettes. Cassettes in this project were CRMD4.0R FLFS of AGFA make. Fourteen Polymethyl methacrylate $(C_5H_8O_2)_n$ blocks commonly known as acrylic or Plexiglas were used to simulate the attenuation of soft tissue. The dimensions of these blocks were 2.54 cm thick, 35.56 cm wide and 43.18 cm long. The blocks were cut to match the size and shape of the CR cassettes. An RTI Black Piranha detector with RTI's Ocean Software was used to determine the HVL for radiography rooms to determine effective energies of polyenergetic beams. This device also measured the tube outputs in mR/mAs so that techniques from one room could determine the necessary mAs values of another room.

After initial trials found it necessary, an additional fourteen acrylic blocks were acquired along with a 7cm x 43.18 cm and 4.445 mm thick 1100 alloy aluminum to account for the additional attenuating effects of the spine. The additional acrylic was needed after reviewing histogram profiles confirmed suspicions that higher EI values were inadvertently obtained due to lack of attenuation, see figure 5. The aluminum addition was prescribed by AAPM Report 31 as a modification to better represent the attenuation of the vertebral column. However, due to the difficulty in obtaining one solid aluminum piece with the specified thickness in the report, seven thinner plates of 0.635 mm aluminum were ordered that summed together nearly matched the report's recommended 4.5mm thickness.

2.3 Procedure

From previously collected data, it was found that general techniques for imaging scoliosis patients were at an SID of 72 inches with 80 kVp and 40 mAs, although the techniques for kVp and mAs were varied. Source to Image Distances were varied to account for patient height. The SIDs to be used were

60, 72, 80 and 90 inches. Peak tube voltages of 75, 80, 85 and 90 kVp were utilized. Tube potential is a factor of patient thickness with the thickest patients requiring the highest kVp settings as higher energy photons are more penetrating of the anatomy. Tube current time product, measured in milliamp seconds (mAs), was adjusted to deliver the EI within the desired target range. The variation of patient size was simulated by varying the thicknesses of acrylic blocks.

The following outlines the procedure for setting up the experiments to determine the appropriate technique to obtain consistent exposure index values within the target EI range.

I. For the series of exposures beginning at 60," the x-ray tube was brought to a source to detector surface distance of 60" from the bottom detector slot. This is where the CR cassette will be placed during exposures. A flat and sturdy surface was placed in front of the scoliboard and the board was adjusted such that the bottom edge of the detector region was flush with the surface.

    1. Two acrylic blocks were then positioned in a portrait orientation one on top of the other flat against the scoliboard. It is highly recommended that the blocks be securely fastened.

   With the acrylic blocks in place, the x-ray tube was positioned where the two acrylic blocks met at the scoliboard. This can be done by either adjusting the laser positioning or the horizontal light field cross-hairs overlays the crevice between the two blocks.

2. The light field was then adjusted to allow a fully open vertical collimation such that the field was evenly distributed between the acrylic. The collimation width was then adjusted such that there could be a noticeable (roughly 2 cm boundary) from the penumbra of the light field and the physical edge of the blocks and scoliboard. Figure 6 shows the final result of this initial setup. It is important to note here that at 60”, the vertical collimation does not reach the bottom edge of the scoliboard and acrylic. The light field covers roughly two thirds of the block. The tube height was not adjusted to accommodate a smaller bottom border between the light field and acrylic.

Figure 3 *Note the width collimation on the bottom block where the penumbra of the light field is positioned within the acrylic. A slight bottom border is also visible. This was collimation adjusted for an SID of 72 inches*.

II. Four additional acrylic blocks were placed in the same configuration overlapping both the top and bottom blocks. The additional 1100 alloy aluminum strip was taped to the surface of the bottom and outermost acrylic block as this would simulate a patient in a PA orientation in congruence with these exams. The aluminum was placed centrally on the acrylic block.

   A. For the five on five (5/5) acrylic configuration, the tube potential was adjusted to be 75 kVp. This potential was used for all SID exposures for the 5/5 acrylic configuration.

      1. From the AGFA console, the following parameters were set for ALL exposures in this experiment:

         a) AGFA protocol of Full Spine AP - As this was the protocol utilized during actual patient examinations.

         b) Large Focal Spot selection - As per patient examinations. It was discovered that using the small focal spot significantly alters the mAs values needed to obtain a suitable EI.

      2. From this point on, the mAs was adjusted and the acrylic exposed with the detector placed on the bottom detector slot. The exposure index value was recorded.

         a) The current time product, mAs, was adjusted until several measurements were found to lie within the target EI range of 400-500. However, due to the at times extreme outliers that present themselves even while using a single CR cassette, the average value was taken of all the exposures and if the majority of recorded EI values were consistent enough to lie within the target range, that mAs value was determined as the appropriate technique for that set up.

B. After the techniques for 5/5 acrylic configuration were determined, the next SID of 72” was tested.

    1. With the same parameters as described before (Full Spine AP protocol and Large Focal Spot selection), the mAs was adjusted until the appropriate target EI values were achieved.
    2. Adjustment of the collimation is required and should follow the same procedure as outlined in I.B. Note that from this point on, vertical collimation for 72, 80, and 90 inch SID’s would need adjusting such that a rough 2cm border is visible along both the bottom edge as well as the sides of the bottom set of acrylic blocks.

III. The remainder of the acrylic configurations involved seven blocks on both top and bottom rows, 7/7. The tube potential was set to 80 kVp to account for more attenuating matter. The procedures for set up and technique determinations are identical to those previously performed in the 5/5 trial.

A. The tube potential was adjusted for higher attenuating material as described in Table 1.

IV. The exposures performed for the remaining acrylic configurations abided by the procedures described above.

Table 1 Selected tube potentials for corresponding acrylic configurations

Acrylic Configuration	Tube Potential [kVp]
8/9	85
10/11	85
9/13	90
11/15	100

Figure 4 Here the configuration is displayed for 8/9 acrylic at 80 inches. Note that the aluminum strip is centrally placed.

Figure 5 *Overview of the experimental set up portraying the techniques for ten blocks placed on top of eleven blocks, 10/11 acrylic configuration with an SID of 72 inches. It was later apparent that more acrylic was necessary to prevent excess scatter from the top row. The 4.445 mm of 1100 alloy aluminum was also added in order to compensate for extra attenuation due to the vertebrae.*

2.5 Conversions of Acrylic to Soft tissue and Room Techniques

Once consistent EI values were obtained within the target range and the established techniques for these results recorded, the next step was to determine the soft tissue equivalence of the average patient to the acrylic. The mass attenuation coefficients were obtained from both Appendix D of Bushberg's Essential Physics of Medical Imaging[12] and from NIST.gov.

A Piranha detector from RTI was used to record both the exposure per mAs as well as the half value layer for each energy of beams that were used in the final technique chart. These were measured with the focal spot to detector distance of 70 cm with the collimation adjusted just outside the edges of the detector. An average of three exposures from 75 kVp, 80kVp, 85kVp, 90kVp and 100 kVp at 10mAs was taken. In order to find the equivalent patient thickness represented in each acrylic and aluminum configurations, the law of exponential attenuation equation was used. Equation 4 becomes:

$$I_o e^{-\left(\frac{u}{p}\right)pt\,\{acrlyic\}-\left(\frac{u}{p}\right)pt\,\{aluminum\}} = I_o e^{-\left(\frac{u}{p}\right)pt\,\{soft\ tissue\}} \qquad \text{Equation 5}$$

rearranging and solving for soft tissue thickness yields,

$$\frac{\left(\frac{u}{p}\right)pt\,\{acrlyic\}+\left(\frac{u}{p}\right)pt\,\{aluminum\}}{\left(\frac{u}{p}\right)p\,\{soft\ tissue\}} = t\,\{soft\ tissue\} \qquad \text{Equation 6}$$

The resulting *t{soft tissue}* yields the equivalent patient thickness to be used for determined techniques.

With the measured tube outputs of another room, it was to be determined if the ratio of tube outputs could accurately predict the techniques of a new room. The tube outputs measured in mR/mAs would determine the mAs needed by taking the ratio of the tube outputs of the two rooms and multiplying them with the mAs of the original room. This assumes that the amount of exposure from one room should produce the same amount of exposure to obtain a similar EI value. The following equation was used to convert the mAs values from one room to another:

$$mAs_C = \frac{mR/mAs_B}{mR/mAs_C} \times mAs_B \qquad \text{Equation 7}$$

The above expression determines the expected mAs technique from room B to room C.

3. Results

Data was collected in radiographic rooms B and C. Room B was designated as the primary room from which room C techniques are based. This chapter is divided into two sections. The first section shows the resultant findings from preliminary investigations highlighting the necessity of additional acrylic blocks as well as the importance of protocol selection. These tests were performed on the ANSI phantom comprised only of acrylic blocks. Section two provides the resultant data of this thesis and provides the final technique charts for both rooms. This data was collected on the modified ANSI phantom that included the 1100 alloy Aluminum described in AAPM report 31.

3.1 Preliminary Data

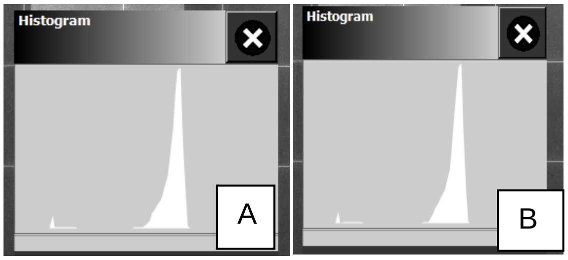

Figure 6 *A) 7/7 Acrylic configuration with techniques of 80 kVp and 125 mAs. B)7/7 Acrylic configuration with techniques of 80 kVp and 100 mAs.*

Figures 6, 7, and 8 show histogram distributions from acrylic configurations. The notation 7/7 refer to the number of acrylic blocks on top and bottom respectively. After more acrylic blocks were acquired, it became necessary to determine the appropriate amount of acrylic to use in both tiers. The use of histograms was used to help aid in determining the appropriate acrylic configurations.

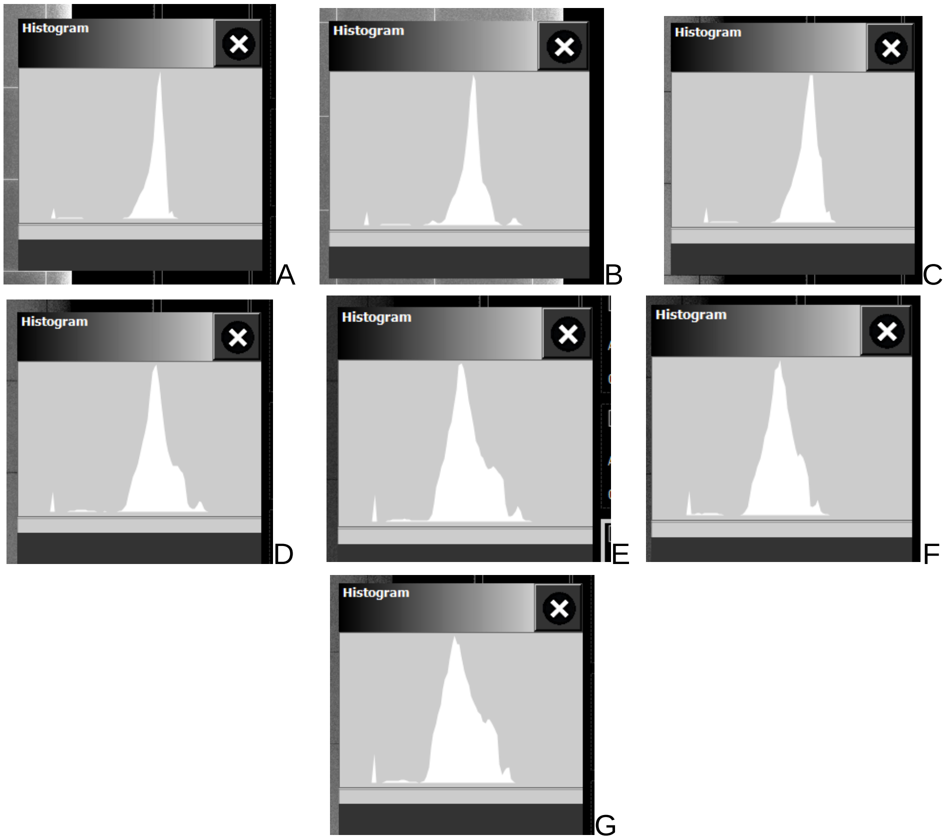

Figure 7 *All configurations were obtained at an SID of 72 inches.*
A) 8/9 acrylic, 85 kVp, 100 mAs EI of 423. B) 5/9 acrylic, 85 kVp, 100 mAs, EI of 394.
C) 11/13 acrylic, 90kVp, 400 mAs, EI of 436. D) 8/13 acrylic, 90 kVp, 400mAs, EI of 494
E) 9/15 acrylic, 90 kVp, 400 mAs, EI of 212. F) 11/15 acrylic, 90 kVp, 400 mAs, EI of 196
G) 11/17 acrylic, 100 kVp, 500 mAs, EI of 206

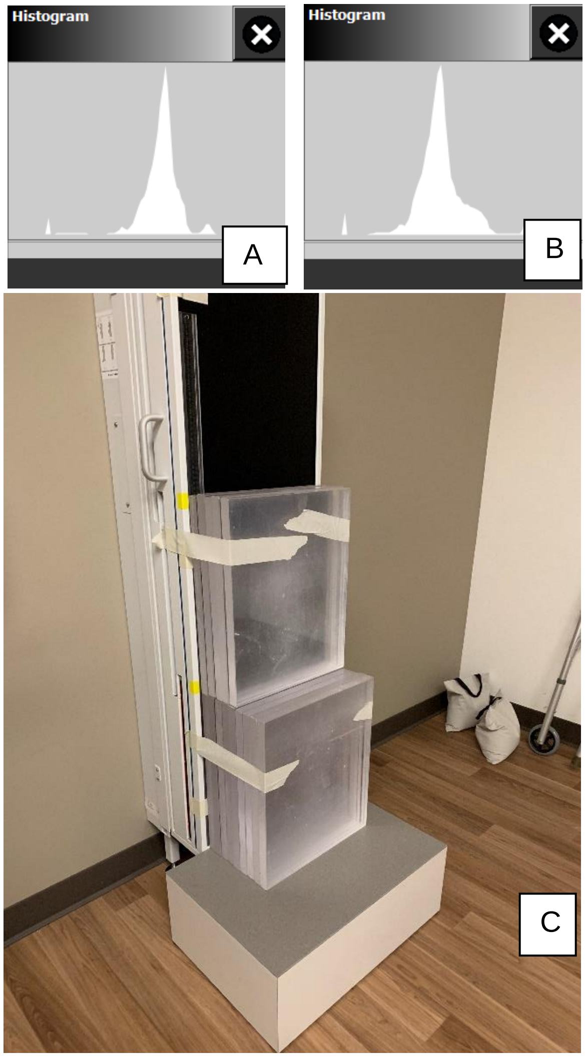

Figure 8 *Both histogram displays share the same techniques. Source to Image distance of 72 inches, tube potential 85 kVp and 80 mAs. A) Histogram distribution for five acrylic blocks on top of nine (5/9). B) Histogram distribution for three blocks on top of eleven (3/11). C) Shows acrylic configuration for 5/9.*

.

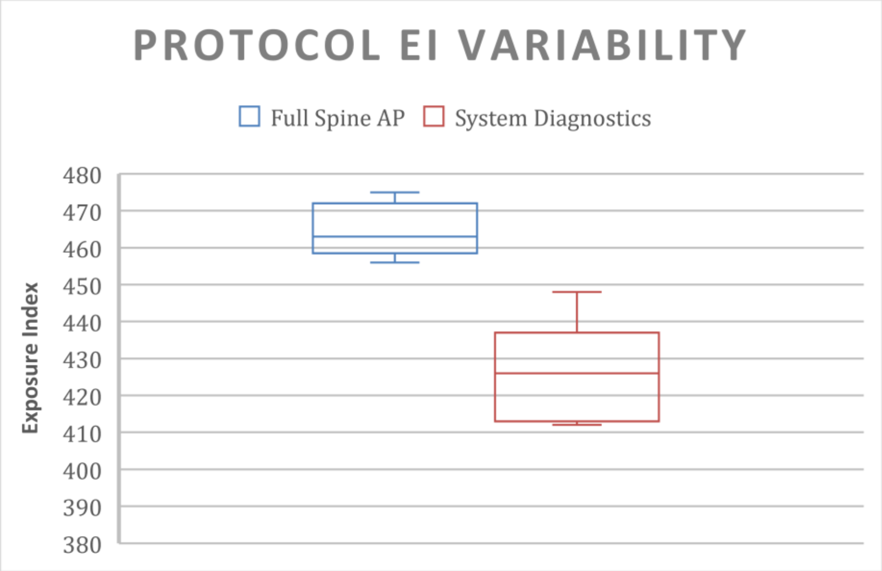

Graph 1 Techniques set at 72" 80 kVp 80 mAs with 7/7 acrylic configuration in Rm B for both protocols. Phantom was composed of acrylic only.

Table 2 Resultant EI values from suitable techniques yielding the best fit for tareget EI range in room B.

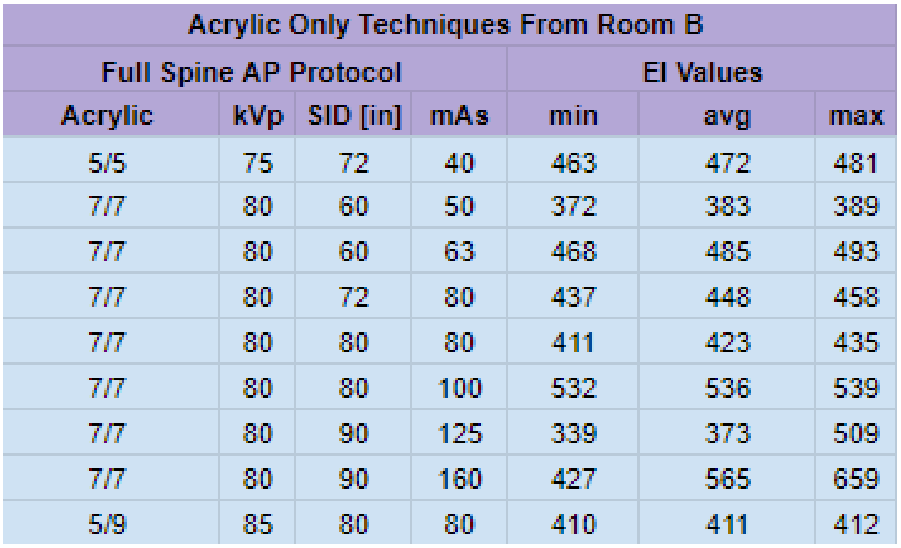

Acrylic Only Techniques From Room B						
Full Spine AP Protocol				EI Values		
Acrylic	kVp	SID [in]	mAs	min	avg	max
5/5	75	72	40	463	472	481
7/7	80	60	50	372	383	389
7/7	80	60	63	468	485	493
7/7	80	72	80	437	448	458
7/7	80	80	80	411	423	435
7/7	80	80	100	532	536	539
7/7	80	90	125	339	373	509
7/7	80	90	160	427	565	659
5/9	85	80	80	410	411	412

3.2 Modified ANSI Phantom Data

Table 3 *Exposure Index results and acceptable techniques in Room B.*

TECHNIQUES FOR ROOM B			**EI Values**			
Acrylic	**kVp**	**SID [in]**	**mAs**	**Min**	**Avg EI**	**Max**
5/5	75	60	32	457	471	495
11.8 cm	75	72	50	406	437	448
	75	80	50	430	432	434
	75	90	63	461	472	484
7/7	80	60	63	452	457	460
16.51 cm	80	72	80	417	432	439
	80	80	100	488	501	540
	80	90	125	390	407	421
8/9	85	60	80	383	410	464
21.3 cm	85	72	100	423	439	449
	85	80	160	383	417	482
	85	90	200	399	408	425
10/11	85	60	160	448	471	485
26 cm	85	72	250	462	487	495
	85	80	320	400	417	436
	85	90	500	182	452	551
9/13	90	60	320	498	501	504
31 cm	90	72	400	474	477	481
	90	80	500	457	459	461
	90	90	630	479	480	482
11/15	100	60	400	468	470	473
35.5 cm	100	72	500	418	420	422
	100	80	630	421	426	432
	100	90	630	716	733	750

Table 4 Room Outputs for Rooms B and C.

kVp	Room B mR/mAs	Room C mR/mAs
75	9.3	10.2
80	10.4	11.8
85	12.2	13.2
90	13.7	16.0
100	17.0	18.3

Table 5 The calculated mAs values for room C based on tube output ratios from both rooms.

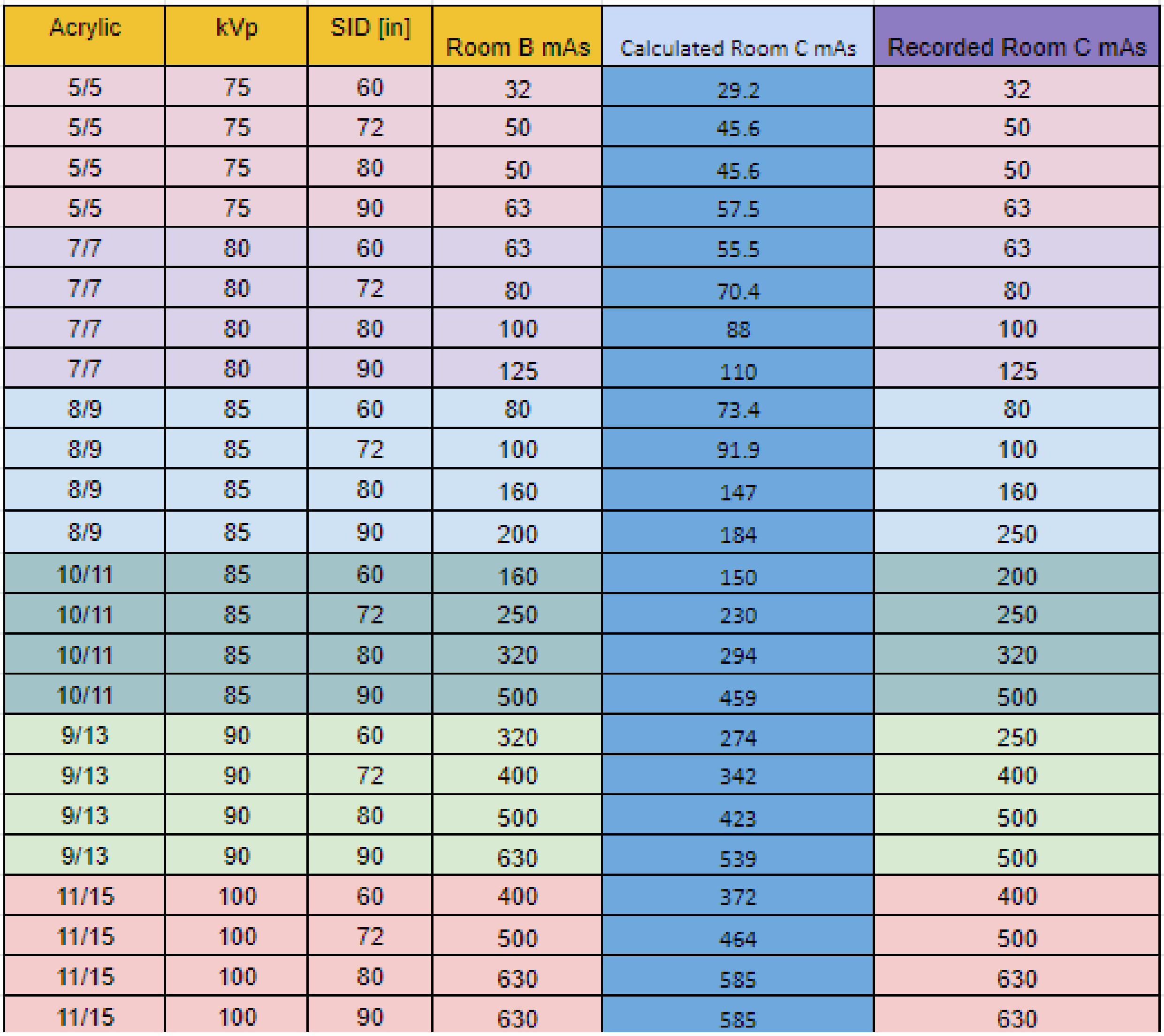

Acrylic	kVp	SID [in]	Room B mAs	Calculated Room C mAs	Recorded Room C mAs
5/5	75	60	32	29.2	32
5/5	75	72	50	45.6	50
5/5	75	80	50	45.6	50
5/5	75	90	63	57.5	63
7/7	80	60	63	55.5	63
7/7	80	72	80	70.4	80
7/7	80	80	100	88	100
7/7	80	90	125	110	125
8/9	85	60	80	73.4	80
8/9	85	72	100	91.9	100
8/9	85	80	160	147	160
8/9	85	90	200	184	250
10/11	85	60	160	150	200
10/11	85	72	250	230	250
10/11	85	80	320	294	320
10/11	85	90	500	459	500
9/13	90	60	320	274	250
9/13	90	72	400	342	400
9/13	90	80	500	423	500
9/13	90	90	630	539	500
11/15	100	60	400	372	400
11/15	100	72	500	464	500
11/15	100	80	630	585	630
11/15	100	90	630	585	630

Table 6 *Resultant techniques displaying acrylic configuration and total lengths for room C along with additional mAs values.*

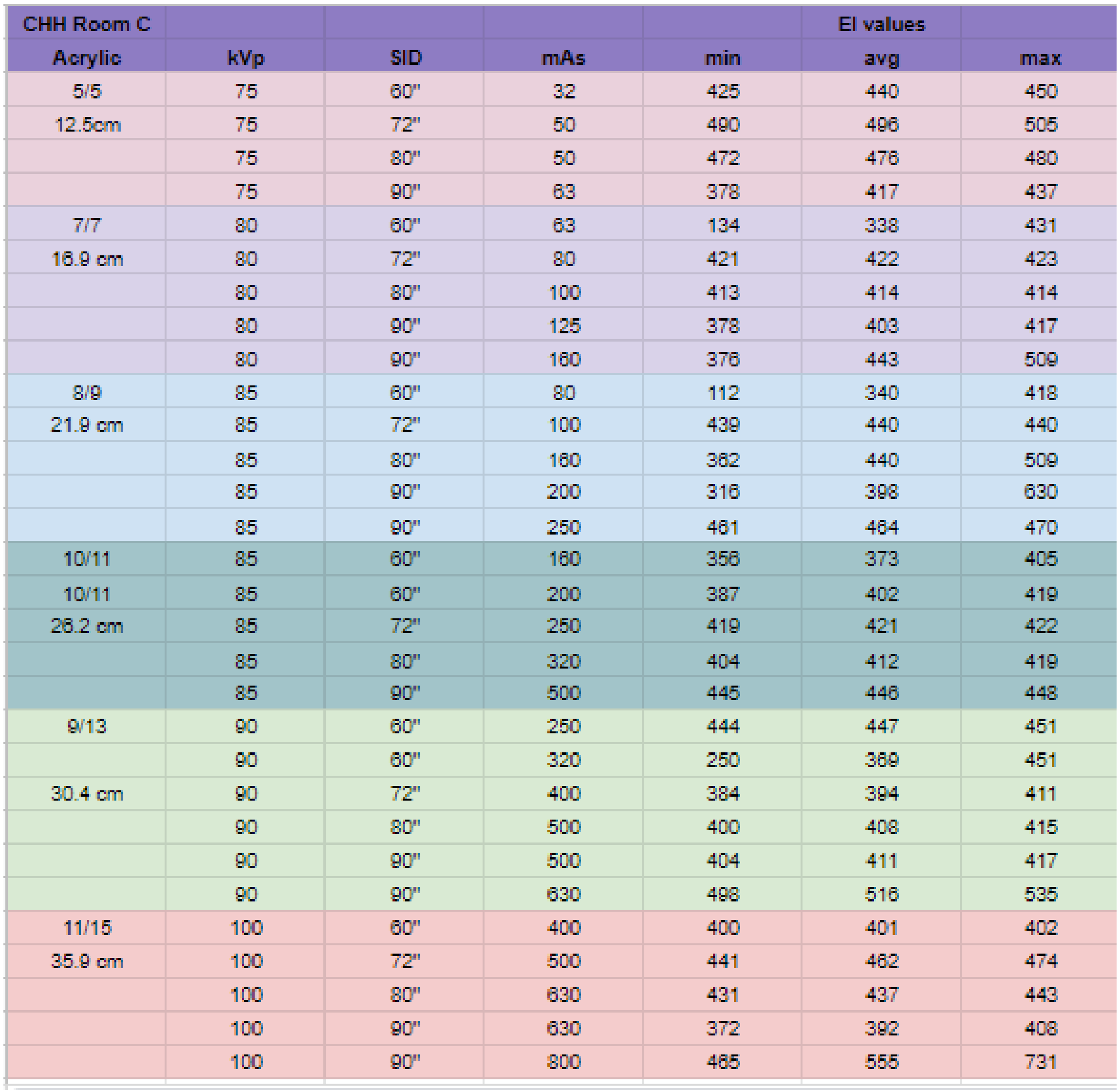

CHH Room C					EI values	
Acrylic	kVp	SID	mAs	min	avg	max
5/5	75	60"	32	425	440	450
12.5cm	75	72"	50	490	496	505
	75	80"	50	472	476	480
	75	90"	63	378	417	437
7/7	80	60"	63	134	338	431
16.9 cm	80	72"	80	421	422	423
	80	80"	100	413	414	414
	80	90"	125	378	403	417
	80	90"	160	376	443	509
8/9	85	60"	80	112	340	418
21.9 cm	85	72"	100	439	440	440
	85	80"	160	362	440	509
	85	90"	200	316	398	630
	85	90"	250	461	464	470
10/11	85	60"	160	356	373	405
10/11	85	60"	200	387	402	419
26.2 cm	85	72"	250	419	421	422
	85	80"	320	404	412	419
	85	90"	500	445	446	448
9/13	90	60"	250	444	447	451
	90	60"	320	250	369	451
30.4 cm	90	72"	400	384	394	411
	90	80"	500	400	408	415
	90	90"	500	404	411	417
	90	90"	630	498	516	535
11/15	100	60"	400	400	401	402
35.9 cm	100	72"	500	441	462	474
	100	80"	630	431	437	443
	100	90"	630	372	392	408
	100	90"	800	465	555	731

After the appropriate mass attenuation values from the acrylic and aluminum have been determined, the soft tissue equivalence accurately represents the actual patient thickness. This was confirmed by comparing the Lucite Aluminum phantom thickness from B.J. Conway's et al. article and comparing the results with the reported patient equivalent thickness[19].

Table 7 *Finalized techniques for Room B to be used in patient examinations.*

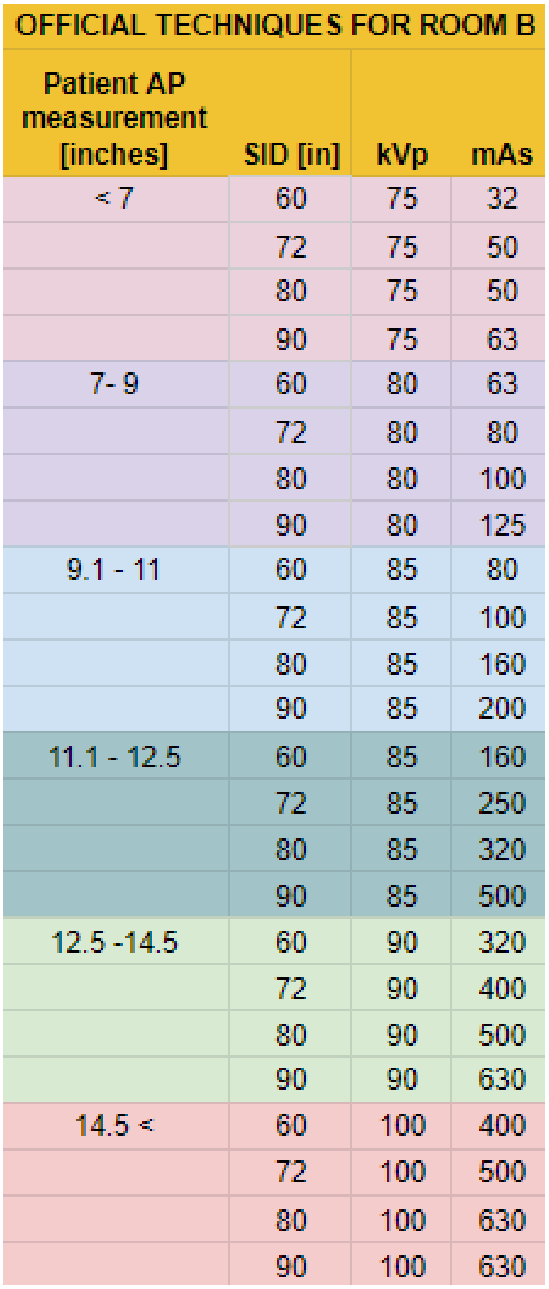

OFFICIAL TECHNIQUES FOR ROOM B			
Patient AP measurement [inches]	SID [in]	kVp	mAs
< 7	60	75	32
	72	75	50
	80	75	50
	90	75	63
7- 9	60	80	63
	72	80	80
	80	80	100
	90	80	125
9.1 - 11	60	85	80
	72	85	100
	80	85	160
	90	85	200
11.1 - 12.5	60	85	160
	72	85	250
	80	85	320
	90	85	500
12.5 -14.5	60	90	320
	72	90	400
	80	90	500
	90	90	630
14.5 <	60	100	400
	72	100	500
	80	100	630
	90	100	630

Table 8. *Finalized techniques for Room C to be used in patient examinations.*

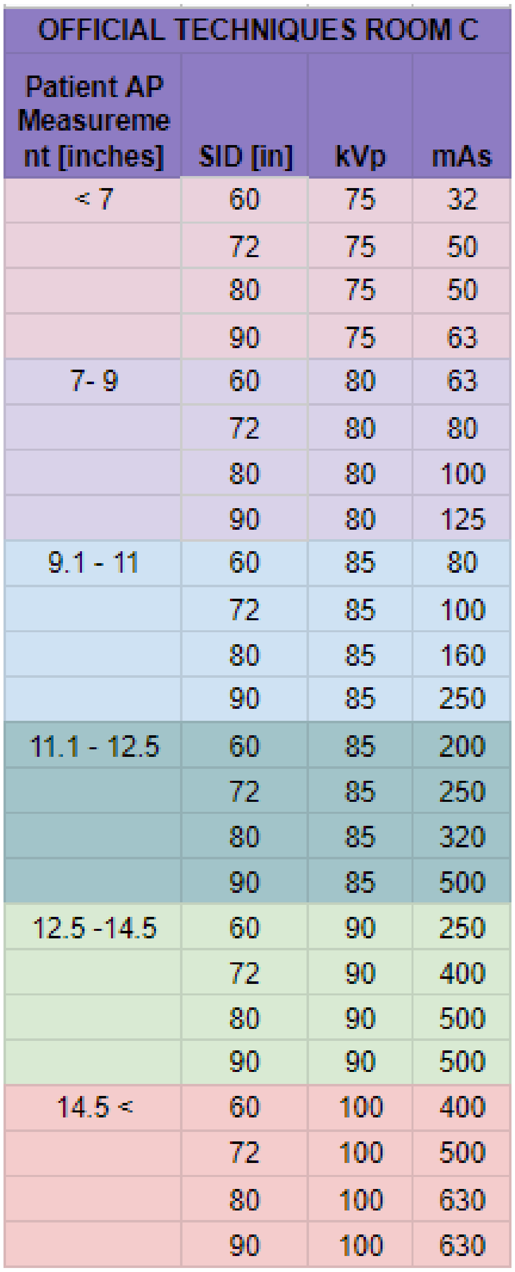

OFFICIAL TECHNIQUES ROOM C			
Patient AP Measurement [inches]	SID [in]	kVp	mAs
< 7	60	75	32
	72	75	50
	80	75	50
	90	75	63
7- 9	60	80	63
	72	80	80
	80	80	100
	90	80	125
9.1 - 11	60	85	80
	72	85	100
	80	85	160
	90	85	250
11.1 - 12.5	60	85	200
	72	85	250
	80	85	320
	90	85	500
12.5 -14.5	60	90	250
	72	90	400
	80	90	500
	90	90	500
14.5 <	60	100	400
	72	100	500
	80	100	630
	90	100	630

4. Discussion

4.1 Preliminary Investigations

Figure 8A depicts the histogram distribution for an acrylic configuration with five blocks placed on top of nine blocks (5/9) while figure 8B represents the histogram for a 3/11 configuration. Both utilized the same techniques of 85 kVp and 80 mAs at an SID of 72” with 5/9 acrylic yielding an EI of 411 and the 3/11 an EI of 866. Note the extended spread of the histogram in figure 8B. This spread was believed to be caused by scatter of the less attenuating portion of the beam incident on the top tier of acrylic resulting in higher EI values.

It was deduced that additional acrylic was necessary to determine the appropriate techniques in order to simulate larger patients. Once the additional acrylic was acquired, it became necessary to determine the amount of acrylic placed on the top tier. This was due to two reasons. One, if the number of top and bottom rows were kept equal, then the maximum acrylic thickness configuration would be limited to fourteen. Two, once the trials reached 13/13 acrylic configurations, the maximum tube output was reached for the farthest SID. In order to determine the appropriate number of acrylic in the top tier, the author decided to utilize the histogram distribution to gauge the appropriate amount of blocks.

The resultant histograms shown in figure 6 show the distributions from the 7/7 configurations with different techniques. Given the characteristic sharp cut-off shape, the author decided it was best not to deviate far from these histogram shapes. Figure 7 illustrates a variety of acrylic configurations. From the figure, it can easily be seen that parts D through G have noticeably wider distributions than those from parts A through C. Comparing C with the 11/13 configuration and D with 8/13, it can be seen that C shows a histogram shape more similar to those from Figure 6. Histogram shapes helped utilize the appropriate number of acrylic blocks to place on the top row.

As shown in Figure 7G, despite reaching maximum tube output, and due to the shape of the histogram distribution, the 11/17 configuration could not be included in this study even with less attenuating acrylic placed on top. The author acknowledges that the use of histogram distribution shape is a qualitative assessment of the exposure reaching the detector. It was assumed that the y-axis of the histogram represented the number of x-rays registered on the detector. The x-axis represents the gray scale values of the image driven by x-ray intensity. There were no indications from the AGFA software as to any numerical metrics for either axes. The author further acknowledges that it can be reasonably assumed that patients would not be best replicated with uniform number of acrylic blocks positioned on top and bottom. A histogram distribution imitating an actual patient examination, may be a more accurate means to determine the appropriate acrylic configurations. However, such information was not available.

Task Group-116, reports that protocols have an impact on the system's algorithm for EI calculation. This was confirmed using a chest x-ray protocol that yielded an EI of 620 for an otherwise acceptable EI value for the exact same acrylic configuration and techniques with a Full Spine AP protocol. Early EI trials were conducted with System CR Diagnostics protocol but were switched to Full Spine Anteroposterior protocols as they are used during an actual scoliosis exam. Graph 1 illustrates the changes of EI values measured with identical set up and technique comparing Full Spine AP and System Diagnostics protocols.

Exposure index variability from protocol selection is due to the specific vendor algorithm in determining the for processing values that will constitute an image. As mentioned in section 1.3, the image segmentation process is the procedure where the vendor determines the relevant image data. As protocols are reflective of the anatomy being imaged, the segmentation process is protocol dependent. As a result of this, different portions of the raw histogram distribution are omitted or utilized thereby adjusting the median Q value resulting in a different display of the exposure index. In addition, certain CR cassettes were clearly seen to yield consistently higher EI values. As a result, the author decided to remove measurement variability from CR cassettes and utilized only one CR cassette for all exposures

It was also found after reviewing TG-31 that a modified ANSI phantom was better suited to represent the human body in radiography. The task group reported that adding 1100 grade alloy aluminum of 7cm width at 4.5mm thickness accounted for the attenuation of the vertebral column. This phantom was subsequently adopted as it was believed that this phantom better simulates the average patient’s interaction with photons in the diagnostic energy range in addition to being spectrally equivalent to the average patient [19].

An additional measurement for a finalized technique chart required measurements of the total thickness of the acrylic blocks themselves. It was realized that while each block was specified to be 2.54 cm thick, there were minor deviations amongst the blocks that when summed together compounded to a significant difference in expected thickness. There was also a noted difference in length and width dimensions of the newly ordered acrylic blocks from the prior set. The author reasoned that the width and height variations were not significant to alter the results of this experiment. This is because the light field was collimated within the confines of the acrylic blocks.

4.2 Modified ANSI Phantom Results

Consistent EI values were successfully obtained for the large majority of techniques. From the preliminary investigations of this project, it was found that utilizing only one CR cassette proved effective in obtaining precise EI values for the same techniques with identical phantom thicknesses. The selection of the appropriate protocol Full Spine AP from System Diagnostics did manifest significant changes and improvements to this project. The addition of the 1100 alloy aluminum did result in a few changes in the mAs settings to consistently produce EI values within the target range. Finally, the method of tube ratios to adjust for techniques between rooms proved to be effective in the majority of scenarios.

Graph 1 shows the importance of protocol selection. As shown from the graph, the average EI value for Full Spine AP was 465 with a minimum value of 456 and a maximum value of 475. System Diagnostics shows a minimum EI value of 412, an average of 425 and a maximum value of 448. This clearly indicates the importance of protocol selection as these drastic changes would lead to inappropriate techniques used by technologists if another protocol is used.

The addition of the 1100 alloy aluminum also contributed to an adjustment of mAs techniques. A quick glance at table 2 shows a technique of 40 mAs at 72” for the 5/5 acrylic yielding suitable EI values, while the aluminum addition required an increase to 50 mAs for the same set up in table 3. The 7/7 acrylic configuration with the ANSI phantom showed 80 mAs at 80” to yield EI values within the target range. The modified ANSI phantom with the addition of aluminum showed that 80 mAs was often just below the target EI range demanding that 100 mAs be used for this set up.

The process of determining the appropriate techniques for a given phantom size and SID were largely successful and yielded results that appeared reasonable. For example, it was expected that higher mAs settings may be needed for larger SID’s with the same phantom thickness. However, the techniques with the maximum phantom size (11/15) at 90” SID, displayed unexpected EI values for Rooms B. As illustrated in table 3, it was expected that when the SID changed from 80” to 90” and using the same technique (100 kVp and 630 mAs), the resulting EI values would be lower at 90” owing to the inverse square law. On the contrary, the resulting EI values were significantly higher. The average EI value was 426 at 80” and 733 at 90.” Table 6 shows the EI results from room C. At the 630 mAs setting for 90,” an expected decrease in EI values was recorded with an average value of 392. Which did show a decrease from the previous set up at 80” which had an average EI value of 437.

The author’s best explanation for these unusual high values from room B are due to excess forward scattering of the beam. This entails an excess incidence of photons on the CR cassette which would lead to a higher exposure index value. The culprit behind this excess forward scatter could be due to the additional layer of acrylic implying harder beam quality as well as broad beam geometry. For room C, 800 mAs used in this scenario resulted in the majority of EI values within the target range. The resultant outlier of 731 was enough to raise the average beyond the target EI range. Despite this suggesting the use of 800 mAs for this configuration, the author advises against this high technique owing to tube failures resulting in premature cessation of exposure. Indeed, room B was unable to produce an exposure with this technique without indicating failure.

The translation of techniques between rooms was mostly successful with only two unexpected results. Room C showed to have a higher tube output over room B as shown in table 4. However, most outputs were within 10% between the two rooms with the most notable exception of the 90 kVp beam. The output of room C was 16.8% higher than that of room B for this technique. Due to the preselected mAs settings, there was limited ability for the author to fine tune the mAs techniques to the calculated values shown in table 5. As a result of these preselected settings, mAs techniques were usually kept the same.

In room C, the 9/13 acrylic configurations at both 60” and 90” utilized the next downgraded mAs setting which were 250 mAs and 500 mAs from room B’s

320 mAs and 630 mAs respectively. This can be seen in table 5. There were only two scenarios for where room C required higher mAs settings than room B to obtain the appropriate EI values. These can also be seen in table 5 and comparing the resulting EI values in table 3 for room B and table 6 for room C. From table 6, the technique of 160 mAs for the 10/11 configuration at 60” yields an EI reasonably close to the target range. The same can be said for the 8/9 configuration when the 200 mAs setting is used. These are the same settings used in room B and very closely yield values at the target range.

The finalized technique charts for both rooms are given in tables 7 and 8. The listed anteroposterior patient thickness measurements for the given techniques are listed the same for both rooms as the equivalent soft tissue conversions were all within the same centimeter. This is a great result for the technologists as they do not need to account for different patient thicknesses corresponding to drastic changes in techniques between these rooms as techniques across both rooms were very nearly identical.

Overall, this project found successful implementation of techniques with only a few unexpected results. These unexpected results were attributed to how the EI is calibrated to an RQA5 beam quality. As the calibrated 70 kVp beam energy is not used in this project owing to large patient sizes, a deviation of the linear proportionality of the detector air kerma is expected. In addition to higher kVp settings, beam hardening due to the acrylic and the aluminum could also contribute to this deviation. In a clinical setting, a visual confirmation is used in conjunction with the resultant EI value in order to determine the adequacy of image quality.

5. Summary and Conclusion

Scoliosis imaging examinations are suitably performed in radiography owing to the adequate image quality to monitor progression and providing diagnostic information [5], [7]. Due to the large portion of anatomy being imaged, a conventional detector is not large enough to capture both the base of the skull and pelvis on the same image for this patient population. For this reason, patients are imaged on a separate scoliboard that has no automatic exposure control or associated technique charts for the technologists to follow. As a result of the lack of assistance to the technologist, scoliosis examinations often have unacceptable noise content or suffer from overexposure.

This project sought to determine if exposure index values could be used as a suitable metric in determining appropriate techniques dependent upon patient size as well as achieving a consistent noise content in these images. The majority of data collected in this project has shown that it is possible to obtain techniques yielding consistent results within a specified target range. Translating those techniques to another x-ray room was successfully based on the tube's output. Therefore, this report concludes that exposure indices are a feasible metric for determining appropriate techniques in scoliosis imaging. With these established techniques, it is reasonable to expect that scoliosis imaging will now have consistent noise content in images and far less variation in exposure index values resulting, in better clinical images overall.

6. Future Studies

Future studies will extend the work of this project into Digital Radiography. Other detectors that directly convert the detector response to an electronic signal without the aid of further light stimulation are referred to as Digital Radiography [1]. These detectors have a higher detective quantum efficiency, meaning that the overall system's capability of converting photon signals from the detector into an image are improved over computed radiography. Since these classes of digital detectors require less exposure to the detector to create a comparable image to CR, the mAs techniques will need to be adjusted to compensate for this improved efficiency.

The methods to determine the appropriate techniques could utilize the same procedure as described in the methods section. As these class of detectors also utilize EI values to determine the amount of radiation reaching the detector, this future study will need to determine the appropriate protocols that the technologists use with this class of detectors. It is expected that the same beam energies for the corresponding phantom thicknesses will remain the same along with utilization of the same source to image distances to account for patient heights. Given the improved detective quantum efficiency, the mAs technique will be expected to be lower for this class of detectors.

Bibliography

[1] J. W. M. van Goethem, L. van den Hauwe, and P. M. Parizel, *Spinal Imaging: Diagnostic Imaging of the Spine and Spinal Cord*. Springer Science & Business Media, 2007.

[2] Hana Kim *et al.,* “Scoliosis Imaging: What radiologists should know,” *Radiographics.,* pp. 1823-1842, Nov-Dec 2010.

[3] “5 Facts about Scoliosis Every Parent Should Know,” 07-Mar-2019. [Online]. Available: https://www.hopkinsmedicine.org/health/articles-and-answers/wellbeing/5-facts-about-scoliosis-every-parent-should-know. [Accessed: 07-Mar-2019].

[4] D. Hoj, J. Elder, and M. Wang, “Principles of growth modulation in the treatment of scoliotic deformities- RS#4,” *Neurisurgey*, pp. 211–221, 2008.

[5] D. Malfair *et al.*, “Radiographic Evaluation of Scoliosis: Review,” *Am. J. Roentgenol.*, vol. 194, no. 3_supplement, pp. S8–S22, Mar. 2010.

[6] “Imaging in Scoliosis: What, Why and How? | Elsevier Enhanced Reader,” 02-Jun-2019. [Online]. Available: https://reader.elsevier.com/reader/sd/pii/S0009926001909092?token=30DAE052FF224EDC7BAA6C359E321DE41FEEB52E2532E3D83A6B5B1B2193A1ABA688C71469CD72548028B6FEA4AA4E8C. [Accessed: 02-Jun-2019].

[7] J. W. M. van Goethem, L. van den Hauwe, and P. M. Parizel, *Spinal Imaging: Diagnostic Imaging of the Spine and Spinal Cord*. Springer Science & Business Media, 2007.

[8] B. K. Potter, M. K. Rosner, R. A. Lehman, D. W. Polly, T. M. Schroeder, and T. R. Kuklo, “Reliability of end, neutral, and stable vertebrae identification in adolescent idiopathic scoliosis,” *Spine*, vol. 30, no. 14, pp. 1658–1663, Jul. 2005.

[9] H. A. King, J. H. Moe, D. S. Bradford, and R. B. Winter, “The selection of fusion levels in thoracic idiopathic scoliosis,” *J. Bone Joint Surg. Am.*, vol. 65, no. 9, pp. 1302–1313, Dec. 1983.

[10] J. E. Pruijs, M. A. Hageman, W. Keessen, R. van der Meer, and J. C. van Wieringen, “Variation in Cobb angle measurements in scoliosis,” *Skeletal Radiol.*, vol. 23, no. 7, pp. 517–520, Oct. 1994.

[11] J. Van Goethem, A. Van Campenhout, L. van den Hauwe, and P. M. Parizel, “Scoliosis,” *Neuroimaging Clin. N. Am.*, vol. 17, no. 1, pp. 105–115, Feb. 2007.

[12] J. T. Bushberg, Ed., *The essential physics of medical imaging*, 3rd ed. Philadelphia: Wolters Kluwer Health/Lippincott Williams & Wilkins, 2012.

[13] F. Attix, *Introduction to Radiological Physics and Radiation Dosimetry*. Wiley-VCH, 1986.

[14] S. J. Shepard, “The Exposure Index for Digital Radiography (IEC 62494-1 and AAPM Report 116),” p. 18.

[15] P. Dewaele, P. Vuylsteke, S. V. de Velde, and E. P. Schoeters, “Full-leg/full-spine image stitching: a new and accurate CR-based imaging technique,” in *Medical Imaging 1999: Image Processing*, 1999, vol. 3661, pp. 131–138.

[16] K. J. Strauss, “Protocol Review and Optimization: Optimization of Pediatric DR,” presented at the 2017 AAPM Spring Clinical Meeting.

[17] J. A. Seibert and R. L. Morin, “The standardized exposure index for digital radiography: an opportunity for optimization of radiation dose to the pediatric population,” *Pediatr. Radiol.*, vol. 41, no. 5, pp. 573–581, May 2011.

[18] R. Fisher and K. Hulme, “Current Implementation Status of IEC Standard 62494-1: Exposure Index (EI) for Digital Radiography,” presented at the 2017 AAPM Annual Meeting.

[19] B. J. Conway, J. E. Duff, T. R. Fewell, R. J. Jennings, L. N. Rothenberg, and R. C. Fleischman, “A patient-equivalent attenuation phantom for estimating patient exposures from automatic exposure controlled x-ray examinations of the abdomen and lumbo-sacral spine,” *Med. Phys.*, vol. 17, no. 3, pp. 448–453, Jun. 1990.

[20] P. Leblans, D. Vandenbroucke, and P. Willems, “Storage Phosphors for Medical Imaging,” *Materials*, vol. 4, no. 6, pp. 1034–1086, Jun. 2011.

[21] E. Seeram and D. Seeram, “Image Postprocessing in Digital Radiology—A Primer for Technologists,” *J. Med. Imaging Radiat. Sci.*, vol. 39, no. 1, pp. 23–41, Mar. 2008.

[22] Shepard, Jeff S., Wang Jihong, *et al.*, "AAPM Report No. 116 An Exposure Indicator for Digital Radiography," American Association of Physicists in Medicine, 2009.

Appendix A X-ray Tube Components

The primary components that compose an x-ray tube responsible for the production of x-rays are the high voltage power supply, cathode, and anode. The purpose of the power supply is to provide an electric potential between the positive potential anode and negative potential cathode stored within the x-ray tube insert. This potential is responsible for the buildup up of electrons on the cathode and depending on the x-ray tube; voltages that range from 20 to 150 kV in diagnostic imaging. The voltages between the anode and cathode are imaging modality dependent. For instance, mammography units have a typical potential range from 25 to 40 kV while radiography utilizes potentials within 40 to 120 kV. Computed tomography makes use of the upper range of potentials in diagnostic imaging. The primary reasons for these distinctions are dependent upon imaging exam parameters such as purpose of the examination and image quality.

The cathode is comprised of both a filament and focusing cup which together serve to release electrons across the vacuum tube and strike the target anode at a specified area defined as the focal spot. The filament is made out of a high melting point metal, tungsten, which is necessary to withstand the high temperatures that the wire is subjected to during the process. Commonly, there are two filaments of different lengths embedded in the focusing cup. The shorter tungsten filament serves as the output for the small focal spot on the anode and the longer filament produces a larger region on the anode to produce the large focal spot of the imaging system. The length of the filament defines the length of the focal spot.

The focusing cup and its voltage (not the voltage potential between the anode and cathode) characterizes the shape as well as width of the focal spot distribution on the anode. As a result of excessive electron accumulation on the cathode surface, specifically the filament, thermal energy within the filament increases because of increased electrical resistance. The point at which the thermal energies of the electrons within the filament exceed the work function of the material results in the escape of the electrons. These freed electrons are no longer bounded by the filament wire and are subjected to the potential between the cathode and anode of the x-ray tube. This process is referred to as thermionic emission. The released electrons are replaced by additional electrons from the current subjected to the filament so that the process is ongoing until the current ceases or the potential on the focusing cup is great enough to prohibit electron ejection as is the case for grid pulsed or grid biased tubes.

Once the electrons are released from the tungsten filament, they are subjected to the voltage potential and are accelerated towards the anode target. The interactions that take place between the electrons and anode target are dependent primarily upon the atomic number of the target material. Given that the target anode is bombarded by numerous electrons, most of the interactions between target atoms and electrons are collisional where most of the energy transferred is lost to heat. Therefore, a high atomic number and high melting point material is desired. Tungsten (Z=74 and melting point = 3,422℃) is the material of choice for a radiography target anode because of its heat capacitance in addition to its resilience to surface damage. Mammography utilizes either molybdenum (Mo, Z=42) or rhodium (Rh, Z = 45) because characteristic x-rays produced from these materials are better suited for the image quality demands from these examinations. Due to high heat energy imparted into the anode, a rotating anode configuration is preferred in order to distribute the heat over a larger surface area which allows for more tube current (the electron flow between cathode and anode) and consequently more x-ray output [12].

Appendix B Photon Interactions

A variety of interactions can occur between the incident electrons and the anode. By far the most common interaction is bremsstrahlung radiation. Known as “braking radiation,” bremsstrahlung radiation is the result of the acceleration of charged particles. Electrons that approach the nucleus of the tungsten target atom are subjected to the Coulombic force of the nucleus where protons alter the trajectory of the electrons as they passes by. Here, the electrons decelerate and their trajectories are altered. The electrons will experience a force inversely proportional to the square of the distance from the nucleus as governed by Coulomb’s Law:

$$F = \frac{q_1 q_2}{4\pi\varepsilon_0 r^2} \qquad \textit{Equation 8}$$

Where ε_o is the permittivity of free space constant, *q1* and *q2* are the magnitude of the charges of two charged bodies, and r^2 denotes the squared distance between the two charged objects. As can be reasoned from the above equation, electrons passing closer to the nucleus, experience a greater electrostatic force.

Therefore, they will experience a greater acceleration translating to a higher release in energy of bremsstrahlung radiation.

Electrons that directly strike the nucleus, experience the greatest deceleration and releases all of its kinetic energy as bremsstrahlung radiation. The probability of electrons interacting with the nucleus increases the farther away they are from the nucleus. Since there are many locations as to where electrons interact with the nucleus,
there is a wide range of bremsstrahlung radiation energy distribution.

Interactions with the anode electron cloud are also possible. From a classical perspective, electrons of a nucleus orbit the nucleus at orbitals. The electrons of the innermost orbits experience a greater electrostatic force with the nucleus than the valence electrons. Electrons have discrete binding energies meaning that only incident electrons from the cathode with sufficient energy are able to eject these orbital electrons. When an incident electron of sufficient energy (i.e. an electron with kinetic energy greater than the binding energy of the orbital electron) strikes this orbital electron, the orbital electron is ejected from the target atom leaving an unstable configuration of the nucleus' electron cloud. To stabilize, an electron from another orbital of the same atom fills this vacancy. In doing so, a photon is released with the energy equivalent to the difference of the orbital shell energies. This is known as a characteristic x-ray and is aptly named due to the fact that every element having a different number of protons in its nucleus has a specific and unique binding energy of its electrons and therefore a photon emission with a unique value that is characteristic of that element. For the purposes of diagnostic imaging, only characteristic x-rays involving the ground state electrons possess adequate energy to serve in imaging.

Other components of the x-ray tube housing include: tube insert, tube port collimators, and tube housing. The tube insert contains the cathode, anode, and rotor assembly (responsible for rotating the anode to reduce the heat load) in a vacuum. The reason for this is to eliminate unwanted electron interactions with air molecules which would reduce the already inefficient process of photon production. The tube port serves to only allow radiation given off to exit the tube in a specified direction and area. The process of bremsstrahlung and characteristic radiation emits photons in all directions but in interest of radiation safety, only photons passing through the tube port are used for imaging purposes. Beyond the tube port, collimators serve to define the field size and boundary of the x-ray field. These are shutters made of lead designed to localize the region where the x-ray field is desired. The purpose of the tube housing is to support and protect the interior components from the outside environment in addition to providing protection to hospital staff from unwanted radiation exposure from photons that are emanated from the anode. This is again done with lead shielding. Lead is an ideal choice for prohibiting photons passage due to the high atomic number which greatly attenuates the photons or stops them altogether [12], [13].

Appendix C COMPUTED RADIOGRAPHY

One type of digital radiography is known as Computed Radiography where photostimulable phosphors or storage phosphors utilize the principles of valence and conduction bands to trap metastable electrons within F-centers so that they may be released later within a CR reader to produce an electronic image [12]. Typical imaging plates are composed of 85% BaFBr and 15% BaFI and are “activated” by the doping of europium to BaFBr. These europium dopants produce F-centers which serve as metastable states for ejected electrons[20].

Once electrons are ensnared within the metastable F-centers, they may remain there for weeks at a time [12]. When a CR cassette is fed into a CR reader, the plate containing the PSP layer is mechanically removed. Then in raster fashion, a red laser of approximately 700 nm wavelength provides enough energy to eject the electrons trapped by the Br^- F-Centers [12]. These electrons then jump back down to the stable energy state of the valence band and as a result a blue light is emitted [20]. An optical filter is in place between the PMT and the PSP plate such that the emissions of blue light (having a shorter wavelength and thus a higher energy than the scanning red laser) pass through into the detector electronics whereas the red laser is prohibited and therefore does not contribute to any of the image processes further downstream in the system [12].

A CR plate is not completely voided of its entrapped electrons with the first few reading scans of the CR reader. In order to clear the CR plate of any residual images, a bright white light with sufficient energy is used to release almost all of the entrapped electrons bringing the entire PSP device back into the ground state so that it may begin the process again for the next imaging exam. Electrons that return to the ground state, reconfigure with the trivalent Eu^{3+} atoms resulting in the original Eu^{2+} dopant [12], [20].